

Supplementary Information

Dual Functional Coordination Interactions Enable Fast Polysulfide Conversion and Robust Interphase for High-Loading Lithium-Sulfur Batteries

Wenchang Han^a, Jiyue Hou^a, Fei Wang^a, Bao Zhang^a, Enfeng Zhang^a, Yongqi Wang^a, Chunman Yang^a, Peng Dong^a, Weili Song^b, Xue Li^a, Yannan Zhang^{a, *}, Shuaifeng Lou^{c, *}, Yingjie Zhang^{a, *}, Yiyong Zhang^{a, *}

^a National local joint engineering research center for Lithium-ion Batteries and Materials Preparation Technology, Key Laboratory of Advanced Batteries Materials of Yunnan Province, Faculty of Metallurgical and Energy Engineering, Kunming University of Science and Technology, Kunming 650093, China

^b Institute of Advanced Structure Technology, Beijing Institute of Technology, Beijing, 100081, China

^c State Key Laboratory of Space Power-Sources, School of Chemistry and Chemical Engineering, Harbin Institute of Technology, Harbin 150001, China

Experimental section

Preparation of electrolyte

The materials and solvents used in this study were obtained from commercial sources such as Aldrich, RHAWN, and Dodochem. The baseline electrolyte consisted of a mixture of two lithium salts: 1 M lithium bis (trifluoromethane sulfonyl) imide (LiTFSI) and 2.0 wt.% LiNO₃, and two solvents, 1,2-dimethyl ethane (DME)/1,3-dioxolane (DOL) (v/v = 1:1). 6-(dibutylamino)-1,3,5-triazine-2,4-dithiol (DTD) was added to the baseline electrolyte at different weight ratios (0.2 wt.%, 0.5 wt.%, 1 wt.%, 2 wt.%, 3 wt.%) and then stirred to form a homogeneous solution. As an example of 1 wt.% concentration, 0.03 g of DTD was added to 2.97 g of baseline electrolyte and mixed well to the optimized electrolyte, and other concentrations can be operated similarly. All preparation processes of this work were performed in an argon-filled glove box with oxygen and moisture content controlled below 0.01 ppm.

Preparation of sulfur cathode

Sulfur-carbon composites were made by mixing 3 g of conductive carbon (Super P) with

7 g of sublimated sulfur in a weight ratio of 3:7. The mixture was ground in a mortar and pestle for 30 minutes to ensure homogeneity. The resulting mixture was placed in a carrier and heated in a tube furnace filled with argon at 155 °C for 12 h. The sulfur-carbon composite, Super P, and binder PVDF were mixed and ground in a weight ratio of 7:2:1. The mixture was dissolved in N-methyl-2-pyrrolidone (NMP), coated onto aluminum foil collectors, and dried in a vacuum oven at 60 °C for 8 h. The dried electrodes were then cut into 12 mm diameter discs. The positive electrode had a sulfur content of 49%. For conventional sulfur loading, the sulfur loading in the paper was approximately 1.2-1.4 mg cm⁻². To prepare the samples for high-loading condition tests, carbon paper was used as the conductive substrate for the positive electrode, and the composite sulfur-carbon material and binder PVDF were mixed and ground with a mass ratio of 9:1, resulting in a sulfur content of 63% in the positive electrode, which was then dissolved in NMP and coated onto the carbon paper, followed by drying at 60 °C for 8 h in a vacuum oven and cutting into 12 mm diameter discs. Celgard 2500 was used as the diaphragm, and lithium metal served as the anode. The electrolyte-to-sulfur (E/S) ratio was fixed at 30 μL mg⁻¹ for conventional loading by adding the baseline electrolyte or an electrolyte containing DTD. For the 3.49-3.54 mg cm⁻² loading, the E/S ratio was also fixed at 30 μL mg⁻¹. For the 5.28-5.38 mg cm⁻² loading, the E/S ratio was 5 μL mg⁻¹. Button cells were assembled using a stainless-steel battery case (Type 2025) in an argon-filled glove box.

Preparation of polysulfides

Sublimated sulfur (Aladdin, 99.5%) and lithium sulfide (Aladdin, 99.9%) were added to the baseline electrolyte in molar ratios of 5:8 and 7:8, respectively. For example, 1.283 g of sulfur and 0.368 g of Li₂S were added to a 0.1 mol L⁻¹ solution of Li₂S₆ in 10 mL of medium baseline electrolyte, the mixed solution was heated and stirred at 60°C for 72 hours. A 0.1 mol L⁻¹ Li₂S₈ was prepared by the above similar method. All operations were performed in an argon-filled glove box.

Electrochemical measurements

During electrochemical performance testing, current multiplication and specific capacity were calculated based on the mass of sulfur in the anode (1 C = 1672 mA g⁻¹). The cycling and multiplication performance of the lithium-sulfur batteries were tested on a Land Test System with a voltage range of 1.7-2.8 V. CV measurements were performed using the LANHE Test

System. The CV measurements were made at a sweep rate of 0.1 mV s⁻¹ over the voltage range of 1.7-2.8 V, and the variable-speed CVs were swept at rates of 0.1, 0.15, 0.2, 0.3, and 0.4 mV s⁻¹. Electrochemical impedance spectroscopy (EIS) measurements and ionic conductivity measurements were performed using an Autolab electrochemical workstation with a frequency range of 100 kHz to 0.01 Hz and an AC excitation signal of 10 mV. Li|S was used for the EIS tests, and a stainless-steel symmetric plug cell was used for the ionic conductivity tests. The constant current intermittent titration (GITT) test was performed on a Neware Test System with a pulsed constant current of 0.2 mA, a relaxation time of 120 s, and a voltage range of 1.6-2.8 V. The GITT test was conducted using a stainless-steel symmetric blocking cell with an AC excitation signal of 10 mV. Ionic conductivity calculations were performed according to the following equation:

$$\sigma = \frac{l}{RA} \quad (1)$$

where σ (mS cm) represents the ionic conductivity, A (cm²) represents the surface area of the electrode, R represents the ohmic impedance, and l (cm) represents the distance between the electrodes.

The diffusion coefficient of Li⁺ during sulfur redox can be measured according to the classical Randles-Sevcik equation:

$$I_p = 2.69 \times 10^{-5} \times n^{3/2} \times A \times D_{Li^+}^{1/2} \times v^{1/2} \times C_{Li^+} \quad (2)$$

where I_p is the peak current, n ($n=2$) is the number of electrons in the reaction, A ($A = 1.13$ cm²) is the electrode area, D_{Li^+} is the Li⁺ diffusion coefficient, v is the scan rate, and C_{Li^+} ($C_{Li^+} = 1 \times 10^{-3}$ mol mL⁻¹) is the Li⁺ concentration in the electrolyte. There is a positive correlation between the slope of the curve and the corresponding Li⁺ diffusion. Based on the linear relationship between $v^{1/2}$ and I_p , the Li⁺ diffusion coefficient of the obtained material can be calculated.

To investigate the effect of DTD on polysulfide conversion and Li₂S deposition, Li|Li₂S₈ and Li|Li₂S₈ + DTD cells (CR2025) were assembled. The anode consisted of lithium foil, the cathode utilized carbon paper, and a Celgard 2500 diaphragm was employed. The Li|Li₂S₈ cell was filled with 30 μ L of 0.1 M Li₂S₈ solution and 15 μ L of base electrolyte, while the Li|Li₂S₈+DTD cell contained 30 μ L of 0.1 M Li₂S₈ solution and 15 μ L of electrolyte with 1 wt% DTD. The cells were discharged to 2.11 V at 0.112 mA and then continuously discharged at

2.09 V to promote nucleation and growth of Li_2S until the current dropped below 10^{-5} A. To determine the redox potentials of DTD and Li_2S_6 , Li_2S_6 +DTD symmetric cells were assembled with lithium foil as the positive electrode and carbon paper as the negative electrode. CV testing was performed at a LAND Test System within a voltage range of 1.7-2.8 V. The CV test was conducted at a LANHE Test System within a voltage range of 1.7-2.8 V. Multiple tests were conducted to ensure data accuracy and reproducibility, while stability was continuously monitored during the testing process.

Characterization

The ^7Li HMR spectra of Li_2S_6 and Li_2S_6 mixed with DTD were analyzed using a nuclear magnetic resonance spectrometer (Bruker 400M). Additionally, characterization of the two substances was performed using a Thermo Fisher Ultraviolet-Visible (UV-vis) spectrometer and a Raman spectrometer (model number LabRAM HR). Photographs were taken for visualization purposes during the experiments. Furthermore, in-situ Raman testing was conducted on lithium-sulfur batteries during charge and discharge cycles using a LabRAM HR Raman spectrometer. Microscopic images of the positive electrode during discharge were also captured. To confirm the reduction of side reactions of polysulfides and lithium anodes by the addition of DTD, the lithium-sulfur batteries were disassembled after 10 cycles. The internal lithium foils were collected, cleaned with dimethoxymethane (DME), and dried in an argon-filled glove box. The surface morphology of the lithium anode was observed using scanning electron microscopy (SEM), and energy dispersive spectroscopy (EDS) was employed for surface examination. Additionally, X-ray photoelectron spectroscopy (XPS) was utilized to analyze the chemical composition of the anode and cathode surfaces after cycling.

DFT modeling

All density functional theory (DFT) modeling was conducted using a Gaussian16 software package, Revision A.03. The geometry optimization of all molecules was performed using the PBE0 functional¹ and Ahlrichs' def2-SVP basis set². Single-point calculations were performed using the def2-TZVP basis set. Grimme's dispersion correction with Becke-Johnson damping³ and the SMD solvation model^[4] were employed in all calculations. Gaussian-type cube files were generated using Multiwfn⁵ 3.8(dev). All Fig.s were rendered using Visual Molecular Dynamics⁶ (VMD) 1.9.3.

Molecular dynamics simulation details

All atomistic molecular dynamics (MD) simulations were performed by the GROMACS 2018.8 simulation package⁷ with the GAFF force field⁸. We generated the atomic charges of anions and solvent molecules by the restrained electrostatic potential fitting procedure (RESP) carried out with the Multifwn software⁵. Topology files and bonded and Lennard-Jones parameters were generated by using the Sobtop. The Packmol package⁹ was used to prepare the initial configuration by randomly distributing desired number of particles in a cubic box with a dimension of 8 nm in length (x), width (y), and height (z). The energy minimization of the whole system was performed using the steepest-descent algorithm. Subsequently, the equilibrium and production simulations were calculated in the NPT ensemble at constant pressure and temperature (298 K) in a cubic box with periodic boundary conditions in all xyz Cartesian direction. For equilibrium processes, the temperature is maintained by V-rescale coupling with a time constant of 0.2 ps. The Berendsen barostat was adopted for controlling pressure. Equilibrium simulation ran 2 ns. For production simulation, the V-rescale coupling and Parrinello-Rahman barostat were used to control the temperature and pressure, respectively. The 20 ns production simulation trajectory was saved every 2 ps for further analysis. The linear constraint solver (LINCS) algorithm was employed to fix all bond lengths. The Particle Mesh Ewald (PME) method was used to calculate the long-range electrostatic interactions. Configurations were visualized using Visual Molecular Dynamics software. Therefore, Radial Distribution Function (RDF) and Coordination Number (CN) data can be obtained by analyzing the results of molecular dynamics simulations. The molecular dynamics trajectory file is read and calculated in the GROMACS program using the post-processing command `gmx rdf`, and the results are obtained by selecting the central and reference atom groups. The value corresponding to each distance r is the average coordination number within that distance and this value can be read directly from the output file.

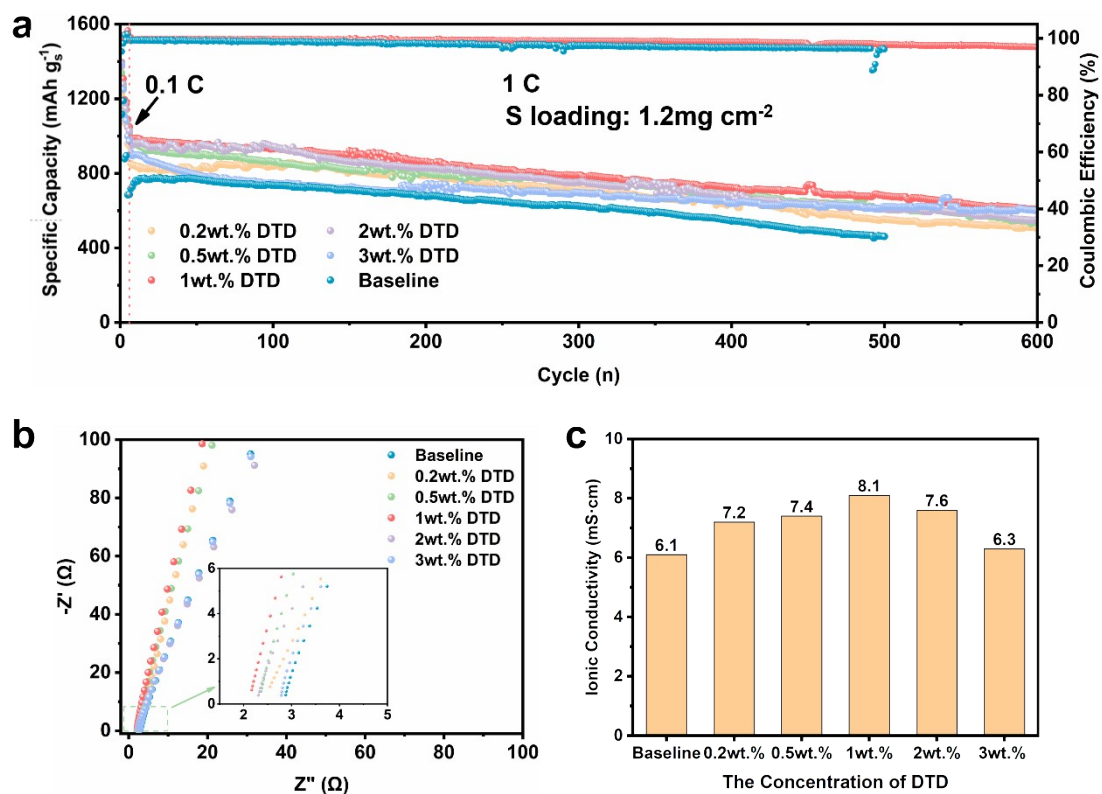


Fig. S1. (a) Cycling performance of cells with different DTD contents at 1 C. (b) Ionic conductivity curves for blocked cell tests with electrolytes of different DTD contents. (c) Comparison of ionic conductivity of electrolytes with different DTD concentrations

Table S1. Impedance and ionic conductivity data obtained by fitting the plots in Fig. S1b

	Impedance (Ω)	Ionic conductivity ($\text{mS} \cdot \text{cm}$)
Baseline	2.80	6.1
0.2wt.% DTD	2.37	7.2
0.5wt.% DTD	2.29	7.4
1wt.% DTD	2.09	8.1
2wt.% DTD	2.23	7.6
3wt.% DTD	2.71	6.3

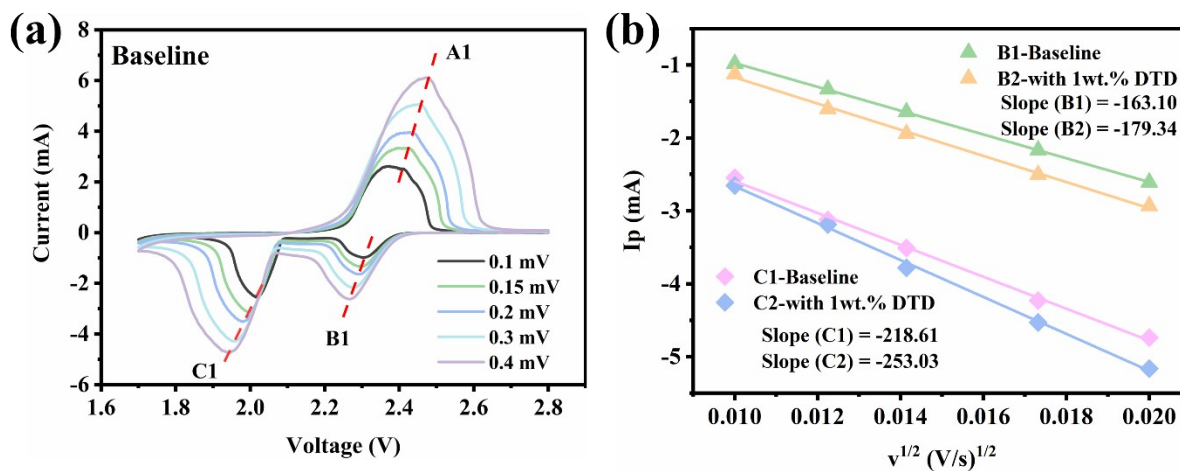


Fig. S2. (a) CV distribution of cells baseline electrolyte at different scan rates. (b) Comparison of I_p - $v^{1/2}$ curves for two electrolyte reduction peaks (peak B and peak C)

Table S2. Lithium-ion diffusion coefficient data calculated based on the R-S equation and I-P- $v^{1/2}$ curves.

D_{Li}	1wt.% DTD	Baseline
Peak A	2.0133E ⁻⁷	1.6295E ⁻⁷
Peak B	4.3437E ⁻⁸	3.5924E ⁻⁸
Peak C	8.6467E ⁻⁸	6.4544E ⁻⁸

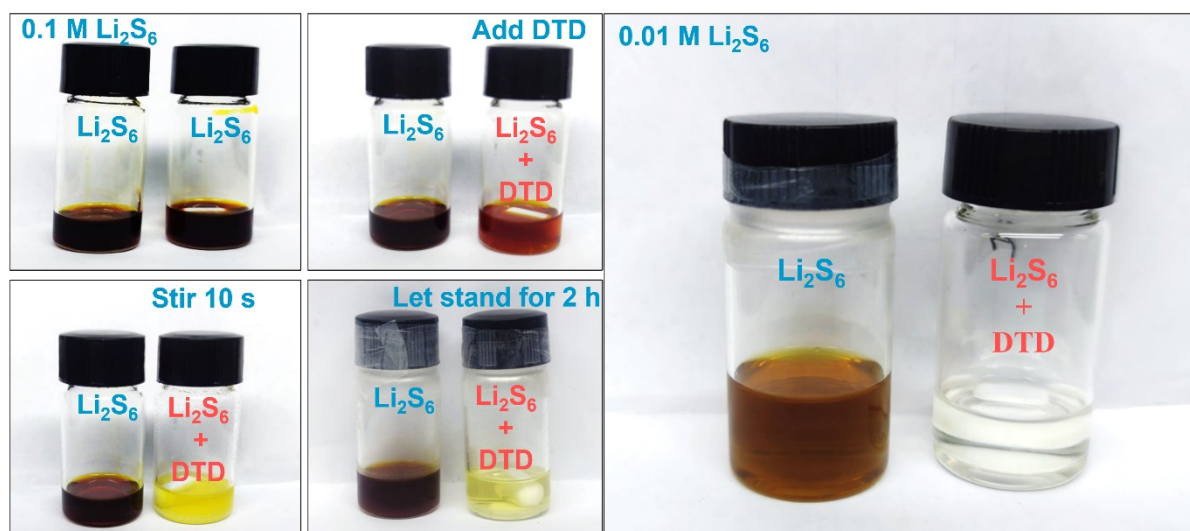


Fig. S3. Visual response phenomena for 0.1 M Li₂S₆ and DTD (left) and visual response results for 0.01 M Li₂S₆ and DTD (right).

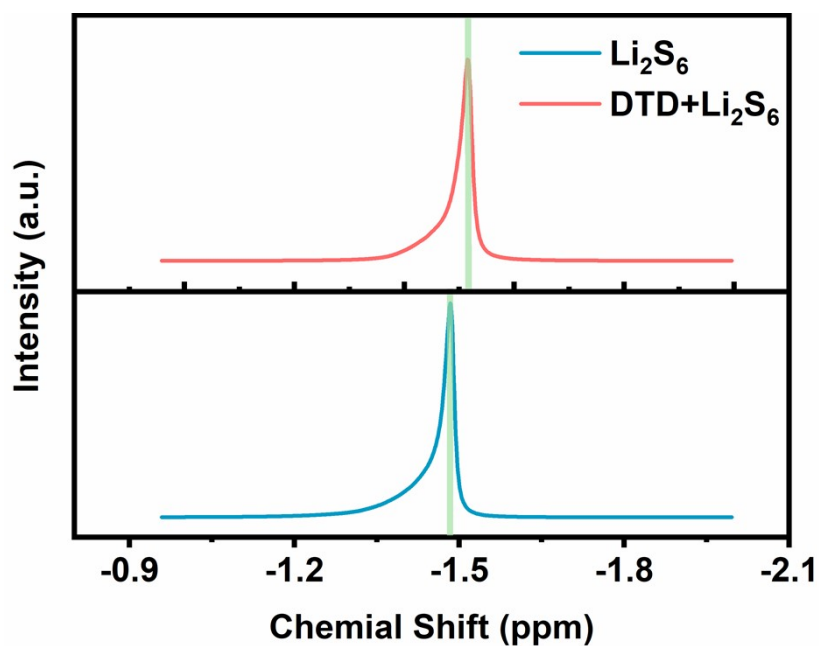


Fig. S4. ^7Li NMR spectra of Li_2S_6 and after addition of DTD to Li_2S_6 .

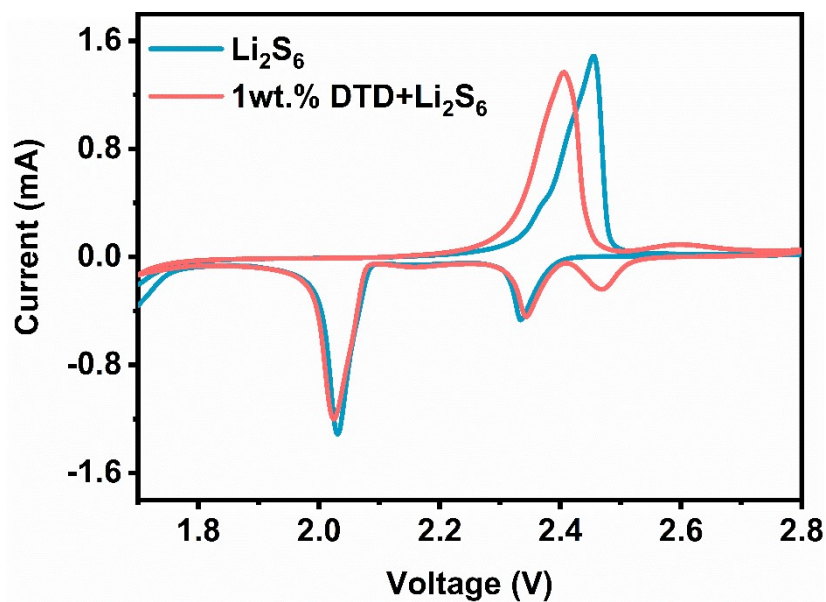


Fig. S5. CV curves of cells using Li_2S_6 electrolyte with/without 1 wt.% DTD with carbon paper as cathode at a scan rate of 0.1 mV s^{-1} .

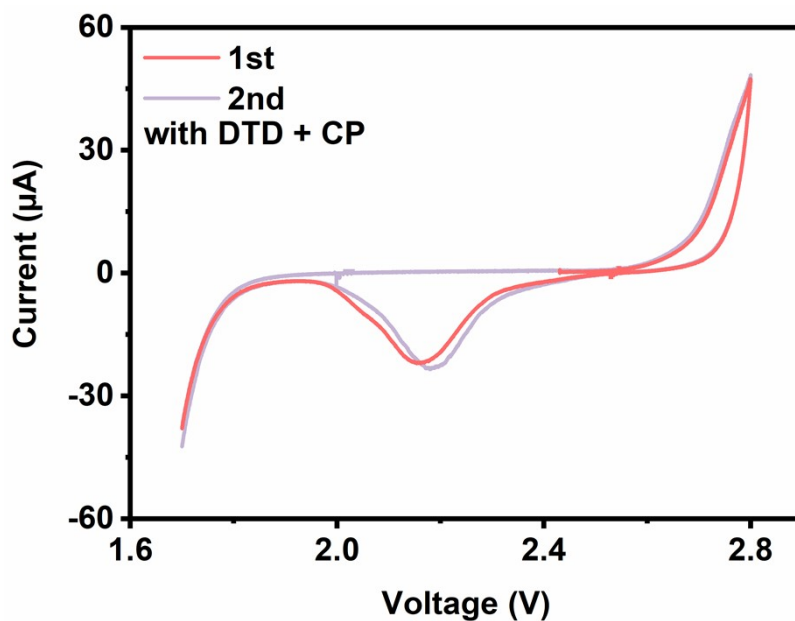


Fig. S6. CV curves of cells using DTD electrolyte with carbon paper as cathode.

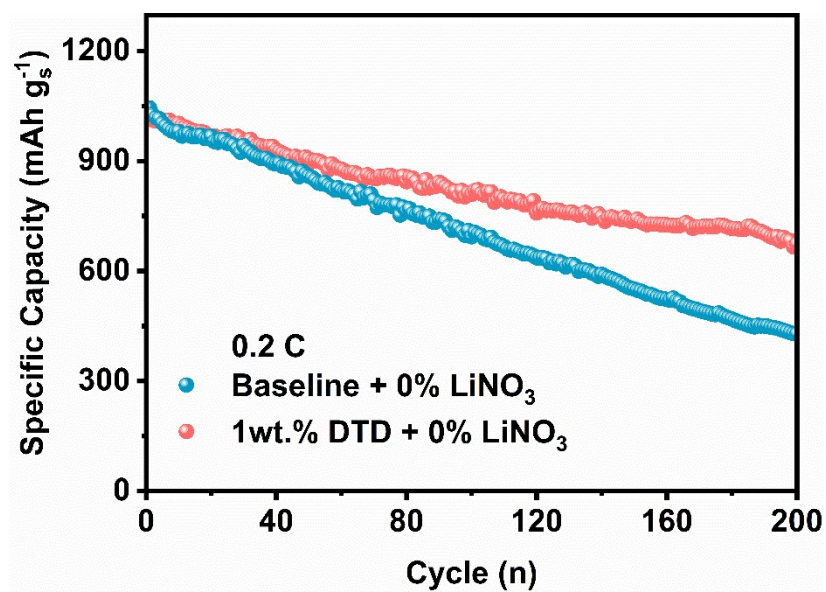


Fig. S7 Cycling performance at 0.2 C of LSBs without and with DTD under the LiNO_3 -free condition.

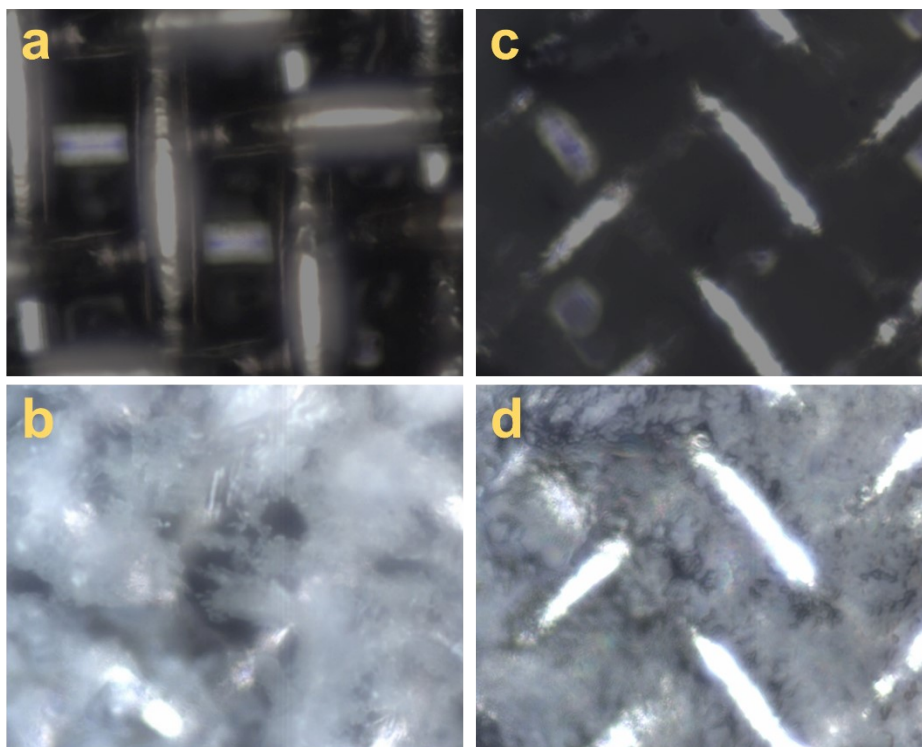


Fig. S8. Sulfur cathode change phenomena collected by microscope during in situ Raman testing (a, b) baseline cell and (c, d) with DTD cell.

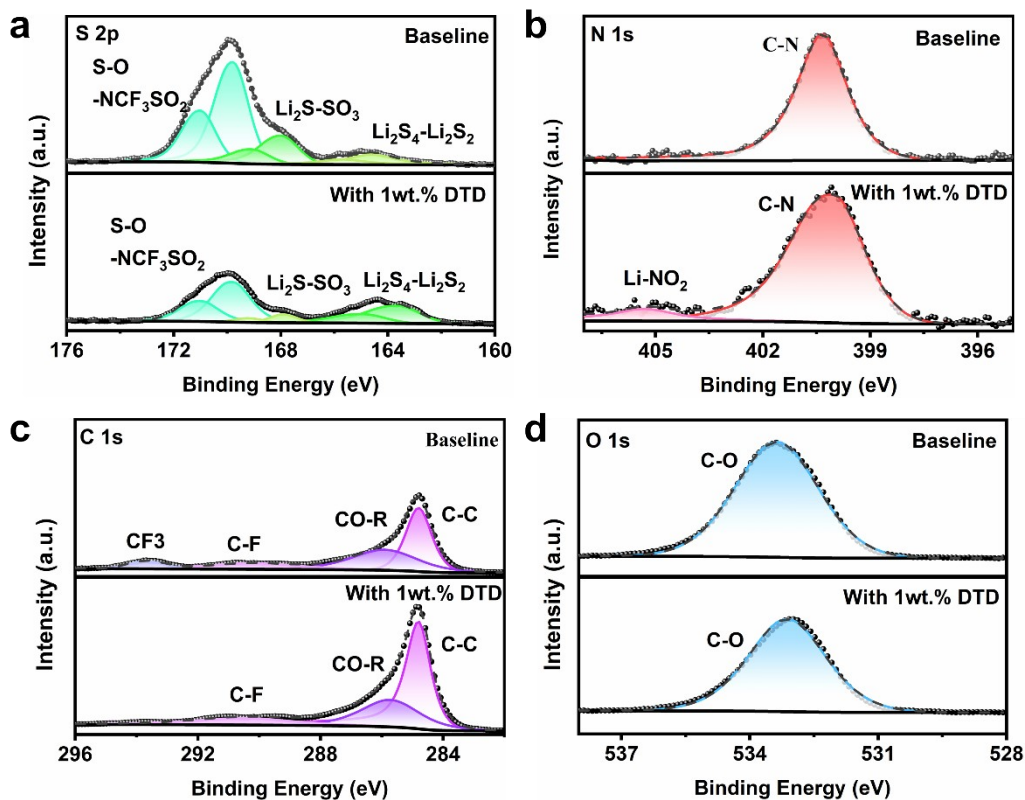


Fig. S9. XPS spectra of S 2p, N 1s, C 1s, O 1s of sulfur cathode after 10 cycles at 0.2 C.

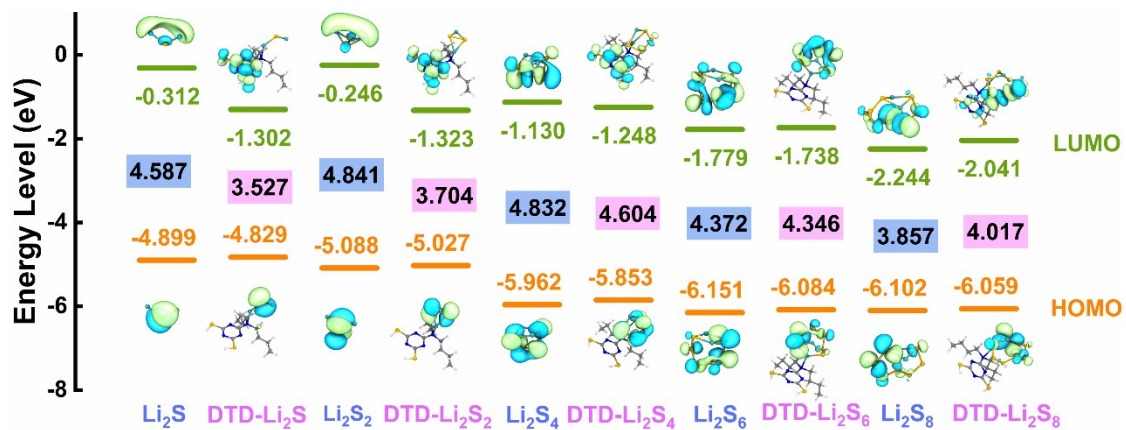


Fig. S10. LUMO and HOMO energy levels of different Li₂S_x species, DTD-Li₂S_x on branched N (Li is green, H is white, C is gray, S is yellow and N is blue).

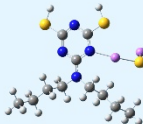
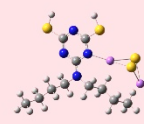
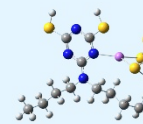
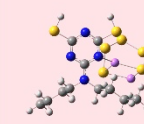


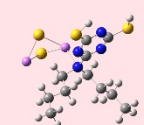
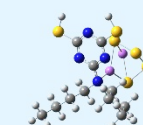
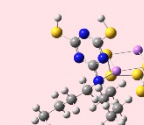
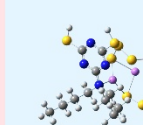
	Li_2S	Li_2S_2	Li_2S_4	Li_2S_6	Li_2S_8
N'	 $\Delta E = -12.60 \text{ kcal mol}^{-1}$	 $\Delta E = -16.68 \text{ kcal mol}^{-1}$	 $\Delta E = -15.71 \text{ kcal mol}^{-1}$	 $\Delta E = -16.70 \text{ kcal mol}^{-1}$	 $\Delta E = -18.42 \text{ kcal mol}^{-1}$
N''	 $\Delta E = -5.36 \text{ kcal mol}^{-1}$	 $\Delta E = -7.19 \text{ kcal mol}^{-1}$	 $\Delta E = -9.02 \text{ kcal mol}^{-1}$	 $\Delta E = -8.80 \text{ kcal mol}^{-1}$	 $\Delta E = -12.58 \text{ kcal mol}^{-1}$

Fig. S11. Relative binding energies (ΔE , kcal mol^{-1}) of the two N atoms on DTD (N' on triazine heterocycle, N'' on branched chain) to Li_2S_x ($x = 1, 2, 4, 6, 8$).

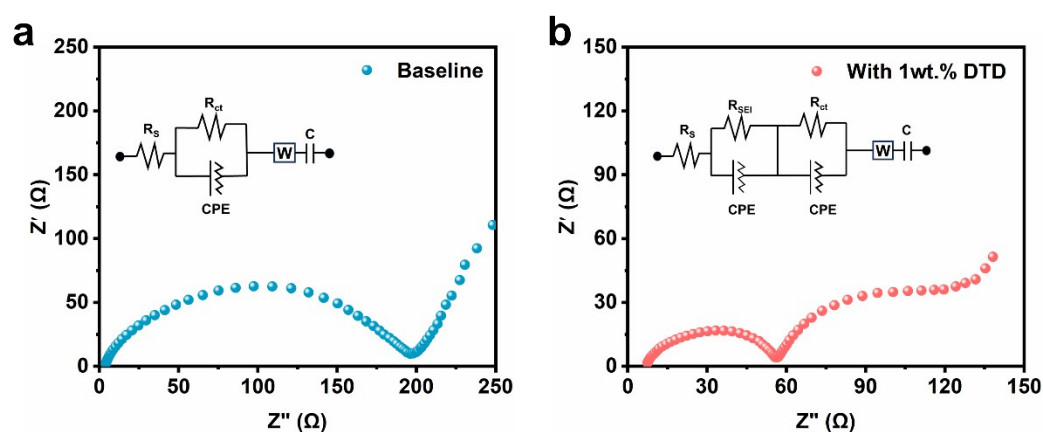


Fig. S12. Electrochemical impedance spectroscopy (EIS) and respective fitted equivalent circuit diagrams of (a) lithium-sulfur battery baseline and (b) with DTD.

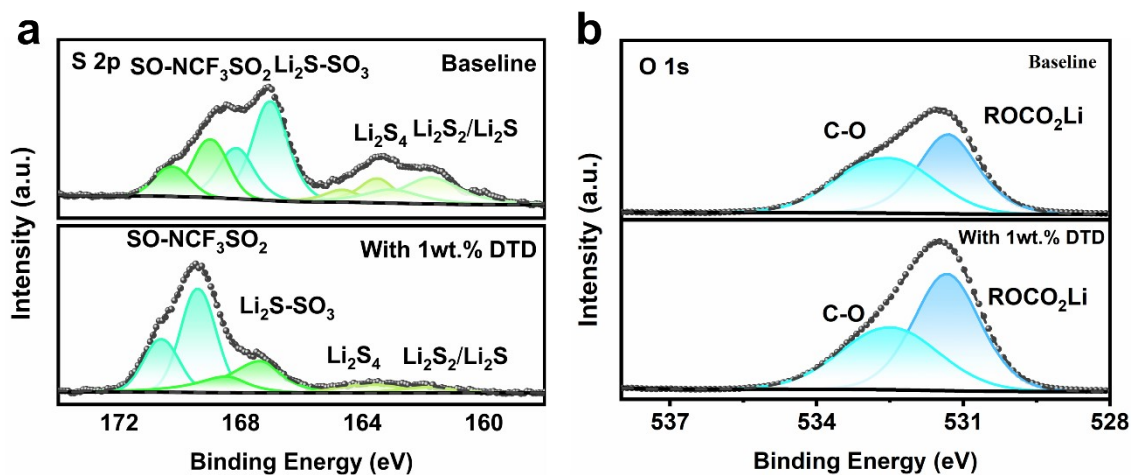


Fig. S13. XPS spectra of S 2p (a) and O 1s (b) of Li anode after 10 cycles of 0.2 C.

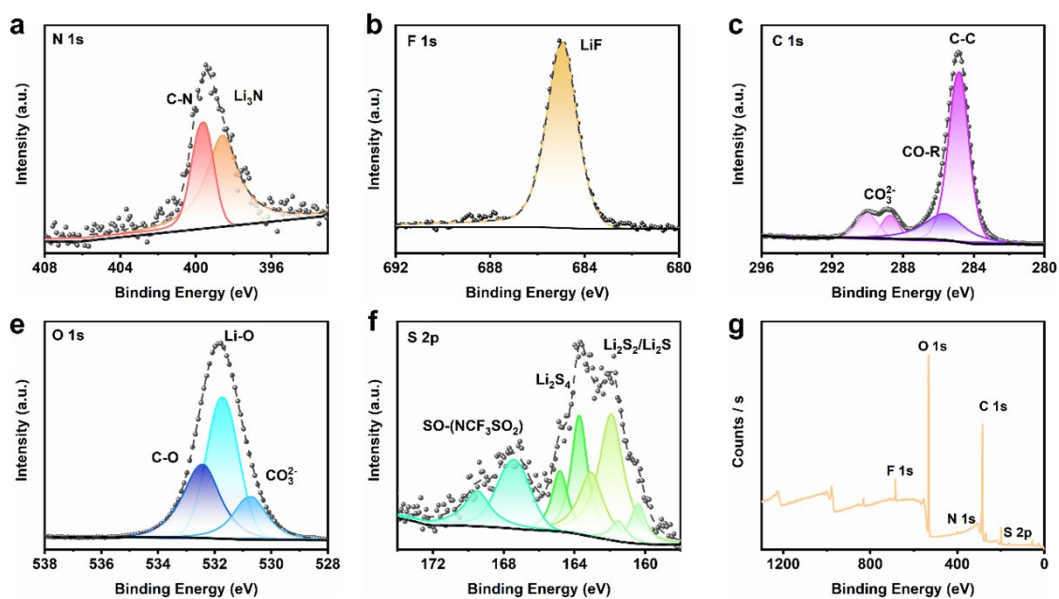


Fig. S14. XPS spectra of N 1s(a), F 1s(b), C 1s(c), O 1s(d), S 2p(e) and the corresponding full spectra(f) on the surface of the lithium anode of a lithium-sulfur battery using DTD in the absence of LiNO_3 after 10 cycles at 0.2 C.

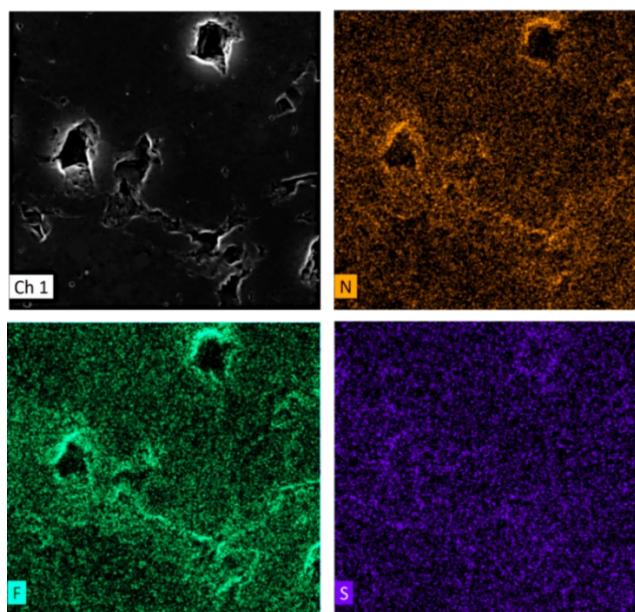


Fig. S15. Energy Dispersive Spectrometer (EDS) of N, F and S elements of the Li anode of a cell after cycling with a DTD additive.

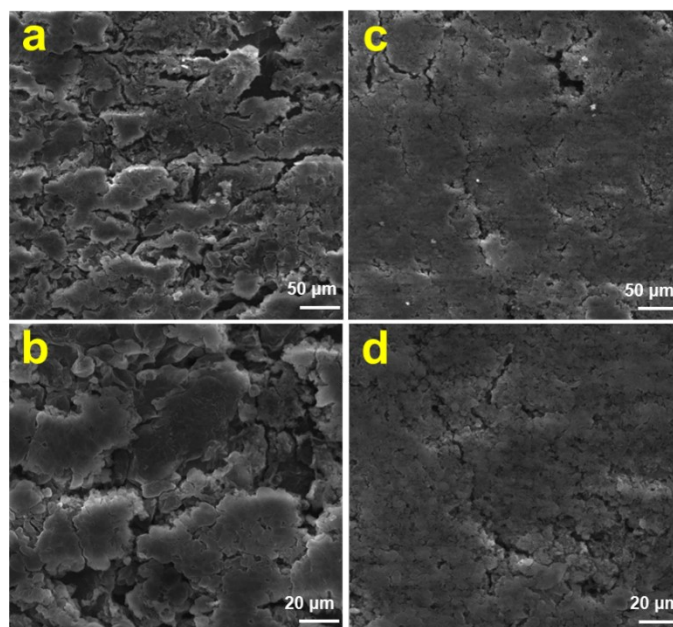


Fig. S16. Scanning electron microscope images at different magnifications of the LSBs anode surface after the end of cycling at 1 C for (a, b) baseline cell and (c, d) with DTD cell.

Table S3. The specific values of the first peak of $g(r)$ and coordination number (CN) for different electrolytes.

	Baseline		With DTD	
	$g(r)$	CN	$g(r)$	CN
$\text{Li}^+\text{-O(DOL)}$	2.152	0.402	2.168	0.323
$\text{Li}^+\text{-O(DME)}$	23.965	3.086	23.034	2.871
$\text{Li}^+\text{-O(TFSI}^-)$	57.23	1.8	60.233	1.831
$\text{Li}^+\text{-O(NO}_3^-)$	145.967	0.635	154.004	0.661

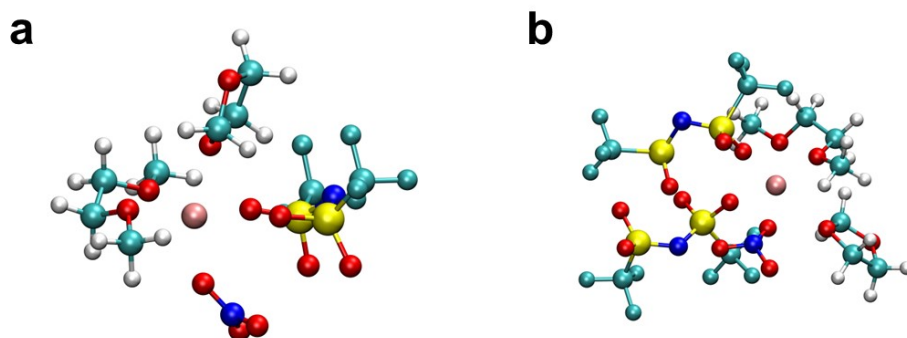


Fig. S17. Li^+ solvation structures of baseline electrolyte (a) and DTD containing electrolyte (b).

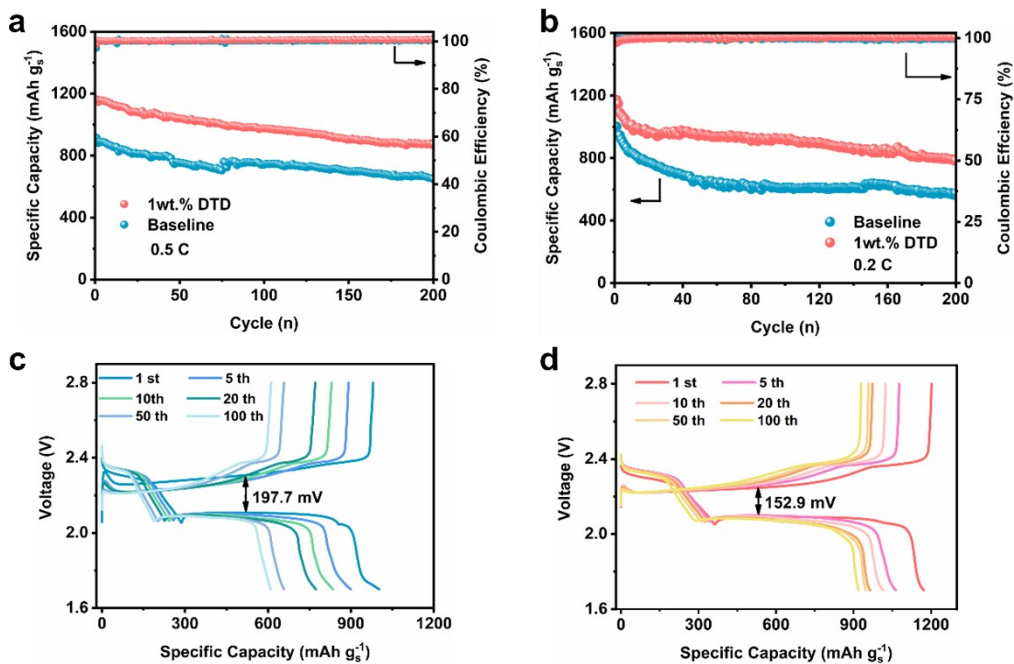


Fig. S18. (a) Cycling performance of LSBs at 0.5 C. (b) Cycling performance of LSBs at 0.2 C. (c, d) Charge-discharge curves of cells without DTD and with DTD electrolyte at 0.2 C with different number of cycles.

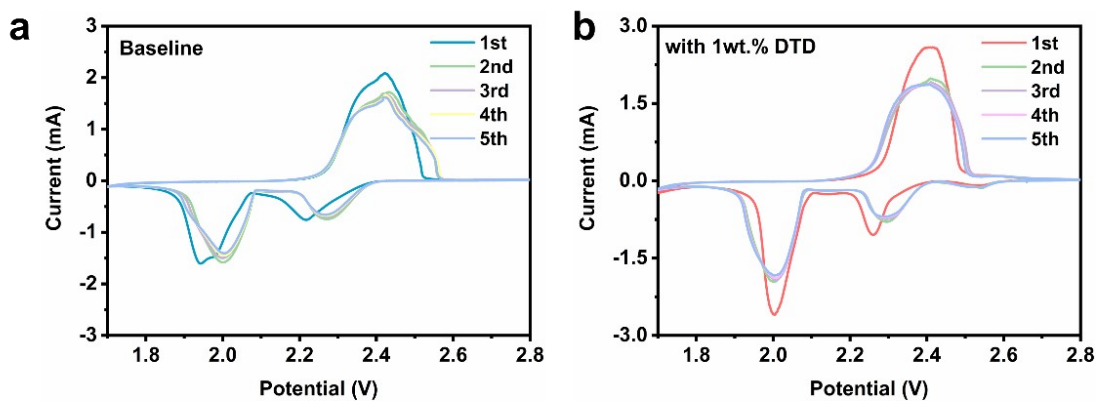


Fig. S19. (a) CV curves for different numbers of turns of the control cell. (b) CV curves of batteries using DTD electrolyte with the different number of turns.

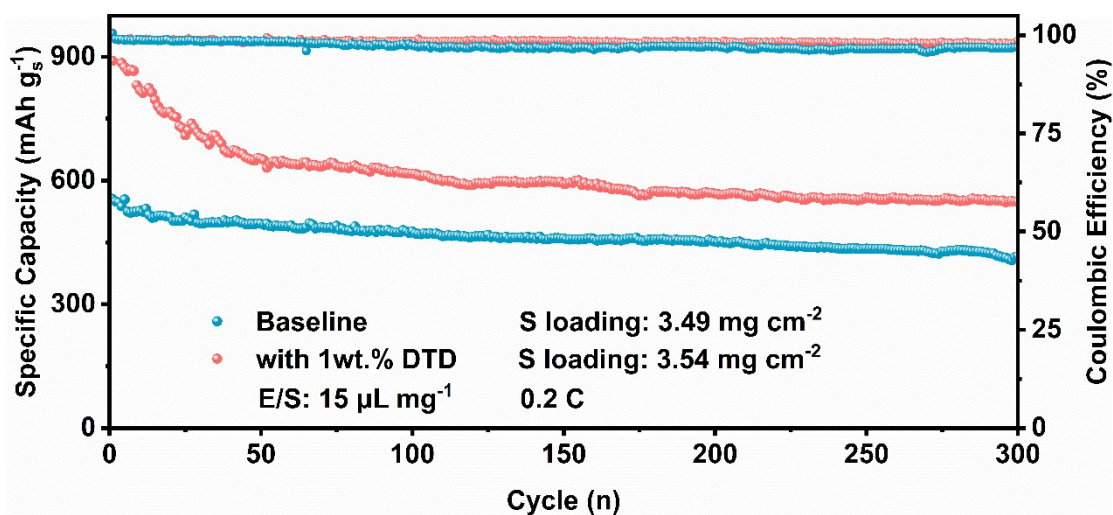


Fig. S20. Cycling performance comparison of LSBs with S loading around 3.5 mg cm⁻² at 0.2 C.

Table S4. Performance comparison of LSBs with different electrolyte additives.

Additive	S-loading (mg cm ⁻²)	Rate	Initial discharge capacity	E/S ratio (μL mg ⁻¹)	Cycle number	Capacity retention rate (%)	Refs.
T ₃ Br	1.5	1 C	898	20	700	65.7	10
	4.6	0.1 C	883	10	100	97	
ZrO(NO ₃) ₂	1.5	0.5 C	1306.2	30	280	63.5	11
Ta/Tta	1.1	0.2 C	1425.5 / 1322.2	30	200	49.4 / 59.4	12
Py	1	1 C	1141.5	35	300	53.2	13

BPD	1	0.1 C	900		300	63.9	14
DODL	1.2	0.5 C	1050	15	350	68.57	15
DMDS _e	4	0.1 C	1010	6.6	130	60	16
DPDS _e	1.2	0.5 C	1056	15.7	350	68.2	17
	5	0.1 C	924	6.8	55	75.7	
DPDT _e	1.2	0.5 C	1227.3	16	300	52.06	18
	5	0.1 C	1142.2	5	100	56.06	
TFA	1.1	0.5 C	1101.2	20	400	61.8	19
	5.2	0.2 C	910	10	150	73.5	
TFMSA	1.2	0.5C	1049	20	350	66.8	20
	5.2	0.2C	972.9	10	100	85.2	
NH ₄ BS	1.2	0.5C	1187.6	20	300	59.65	21
	5.6	0.2C	880	10	196	72.6	
DTD	1.2	0.5C	1164	30	200	75.1	
	1.2	1C	990.1	30	600	61.3	This work
	5.38	0.2C	663.7	5	290	71.5	

References:

1. C. Adamo and V. Barone, *J. Chem. Phys.*, 1999, **110**, 6158-6170.
2. F. Weigend and R. Ahlrichs, *Physical Chemistry Chemical Physics*, 2005, **7**, 3297-3305.
3. S. Grimme, S. Ehrlich and L. Goerigk, *J. Comput. Chem.*, 2011, **32**, 1456-1465.
4. A. V. Marenich, C. J. Cramer and D. G. Truhlar, *J. Phys. Chem. B*, 2009, **113**, 6378-6396.
5. T. Lu and F. Chen, *J. Comput. Chem.*, 2012, **33**, 580-592.
6. H. S. Fernandes, S. F. Sousa and N. M. F. S. A. Cerqueira, *JCIM*, 2019, **59**, 4519-4523.
7. M. J. Abraham, T. Murtola, R. Schulz, S. Páll, J. C. Smith, B. Hess and E. Lindahl, *SoftwareX*, 2015, **1-2**, 19-25.
8. J. Wang, R. M. Wolf, J. W. Caldwell, P. A. Kollman and D. A. Case, *J. Comput. Chem.*, 2004, **25**, 1157-1174.
9. L. Martínez, R. Andrade, E. G. Birgin and J. M. Martínez, *J. Comput. Chem.*, 2009, **30**, 2157-2164.
10. R. Meng, X. He, S. J. H. Ong, C. Cui, S. Song, P. Paoprasert, Q. Pang, Z. J. Xu and X. Liang, *Angew. Chem. Int. Ed.*, 2023, **62**.
11. J. Li, L. Zhang, F. Qin, B. Hong, Q. Xiang, K. Zhang, J. Fang and Y. Lai, *J. Power Sources*, 2019, **442**.
12. D.-Y. Wang, W. Wang, F. Li, X. Li, W. Guo and Y. Fu, *J. Energy Chem.*, 2022, **71**, 572-579.
13. W. Yang, W. Yang, A. Song, L. Gao, G. Sun and G. Shao, *J. Power Sources*, 2017, **348**, 175-182.
14. H.-L. Wu, M. Shin, Y.-M. Liu, K. A. See and A. A. Gewirth, *Nano Energy*, 2017, **32**, 50-58.
15. J. Gu, C. Shi, Z. Li, F. Liu, Z. Huang, B. Hong and Y. Lai, *Chem. Eng. J.*, 2022, **432**.
16. Y. Liu, M. Zhao, L.-P. Hou, Z. Li, C.-X. Bi, Z.-X. Chen, Q. Cheng, X.-Q. Zhang, B.-Q. Li, S. Kaskel and J.-Q. Huang, *Angew. Chem. Int. Ed.*, 2023, DOI: 10.1002/anie.202303363.
17. M. Zhao, X. Chen, X.-Y. Li, B.-Q. Li and J.-Q. Huang, *Adv. Mater.*, 2021, **33**.
18. W. Zhang, F. Ma, Q. Wu, Z. Zeng, W. Zhong, S. Cheng, X. Chen and J. Xie, *Energy Environ. Mater.*, 2022, DOI: 10.1002/eem2.12369.
19. L. He, S. Shao, C. Zong, B. Hong, M. Wang and Y. Lai, *ACS Appl. Mater. Interfaces*, 2022, **14**, 31814-31823.
20. F. Liu, C. Zong, L. He, Z. Li, B. Hong, M. Wang, Z. Zhang, Y. Lai and J. Li, *Chem. Eng. J.*, 2022, **443**.
21. J. Gu, D. Yang, X. Wang, Y. Song, Z. Li, H. Qiu, M. Wang, Q. Wang, B. Hong, Z. Zhang, J. Li and Y. Lai, *J. Colloid Interface Sci.*, 2023, **629**, 368-376.